JOURNAL OF MATERIALS SCIENCE 32 (1997) 4513–4521

Preparation and characterization of alumina–iron cermets by hot-pressing of nanocomposite powders

J. L. GUICHARD, O. TILLEMENT, A. MOCELLIN
LSG2M-U.R.A. 159-Ecole des Mines, Parc de Saurupt-54042 Nancy Cedex, France

Alumina composites with 0–36 vol% iron metal dispersed inclusions have been prepared by a new processing route. Nanostructured powders were synthesized by a high energy dry ball-milling process and then consolidated by sintering at 1700 K under a pressure of 30 MPa. The materials consist of micrometre-size Al_2O_3 with metallic Fe in isolated regions from 10 μm down to nanometre size. From low to high metallic contents, the same type of interwoven microstructure is observed. Hardness, elastic and shear moduli, fracture toughness and the size of the inclusions vary regularly with the metal content. Addition of metal increased the fracture toughness from 3.0 to 8 MPa $m^{1/2}$.

1. Introduction

The idea of incorporating a ductile metallic phase in order to improve the toughness of brittle ceramics is not new and has been successfully applied to several systems. Among this type of materials, often called cermets, alumina based ceramics have been widely investigated. The first metallic dispersions used in alumina were chromium particles [1, 2]. Since then, alumina matrices have been toughened by other popular metallic inclusions such as aluminium [3], molybdenum [4, 5], iron [6], nickel [7–9] and silver [10].

The toughening mechanisms have already been investigated [11, 12] and the enhancement is believed to be produced by the plastic inclusions which bridge the crack and are stretched as it opens, absorbing energy which contributes to the toughness. Nevertheless, some interface conditions have to be fulfilled in order for the plastic deformation to be fully exploited and the particle shape and particle-matrix bond strength are two important parameters [13]. The metallic inclusions need to be firmly bonded to the brittle matrix and need to be kept with a particular geometry below the critical size at which thermal stresses become sufficient to induce cracks around the metal particles [14, 15]. If the interface bonding strength is too weak, cracks will propagate along the interface and plastic stretching of the ductile reinforcements will not occur.

On the other hand, if the bonding between ceramic and metal is very strong (a rare case), the extent of inclusion deformation will be limited resulting in limited toughness increase [11]. Therefore, in a metal reinforced ceramic-composite the fracture toughness can be enhanced by optimizing the metal/ceramic interface behaviour. This strongly depends on both the choice of the ductile phases, and the processing method used [16].

Two main difficulties in the metal-ceramic composites still remain and restrict their use for structural application: first the poor interfacial cohesion between the metallic particles and the ceramic matrix and second the highly non-uniform and large metallic particles dispersion often associated with a high content of pores [8], large amounts of metal phase often interfere with the sintering mechanisms. Recently it has been proposed to reduce such unfavourable characteristics by a reduction of the mean grain size to the nanometre region [17, 18]. Both, the achievable regularity of metallic dispersion and the interfacial cohesion may be affected by a reduction of the grain size.

In this context, a rather simple technique for preparing nanometre-sized alumina-metal composites is the mechanosynthesis of powders by high-energy dry ball milling [19, 20]. The synthesis is performed by a solid state reduction reaction which occurs during room temperature milling of mixtures of a metal oxide (M_xO_y) and (2y/3 Al). Mechanical activation can induce the reduction reaction. After an appropriate time which depends on the physico-chemical conditions of the milling experiments, the reaction products consist of agglomerates of very fine crystallites (about 10 nm) with a high defect density and interfacial content [21]. Such powders exhibit a composite structure with homogeneous distribution of metal and ceramic phases in the nanometre ranges.

The objective of the present study was to densify such powders in order to prepare monolithic ceramic-metal composites with a fine scale homogeneity. As a model system, Fe dispersions in Al_2O_3 have been studied with the metal phase content reaching 36 vol%.

0022–2461

2. Experimental procedures

2.1. Sample preparation

The starting powders were commercially available aluminium (Ecka AS 011), alumina (Martinswerk HRA-5) and iron oxide (Riedel de Haen). Average particle sizes of these powders were in the micrometre range. The as-received atomized aluminium was oxidized on its surface and the typical alumina content was 0.5–1 wt%. The reaction which takes place during the ball-milling is as follows:

$$2x\mathrm{Al} + x\mathrm{Fe_2O_3} + (1-x)\mathrm{Al_2O_3} \rightarrow \mathrm{Al_2O_3} + 2x\mathrm{Fe} \quad (1)$$

The contents of iron in the selected composition have been chosen in the range of $x = 0$–1 which is the stoichiometric composition of the oxydo-reduction reaction. This corresponds to a volume fraction of metallic phase of 0–36 vol%.

High energy milling was carried out in a planetary ball-mill (Fritsch Pulverisette 7) under an argon atmosphere. The grinding media (7 balls of 20 mm diameter and vials) were hardened chromium steel. Stoichiometric mixtures of Fe_2O_3 and Al with the adjusted excess alumina were milled for 8 h with a powder-to-ball ratio of 1:20. As identified from the X-ray diffraction patterns, α-Al_2O_3 and Fe were the two main compounds with a small content (<2%) of hercynite $FeAl_2O_4$, also being observed [20]. Fig. 1(a and b) shows the morphology and the microstructure of typical mechanosynthesized powder particles. After such high reactive milling, nanometre sized crystallites are produced from the initial micrometre sized powders. The particles consist of finely divided aggregates of crystallites 2–30 nm in size with an extremely high defect density due to the mechanical action [21] and the powder nanostructure [18]. The mean crystallite size, as estimated by X-ray line broadening [22] lies around 10 nm for the ceramic phase. The transmission electron microscopy (TEM) observations give the same average size for the metallic crystallites. The corresponding particles appear as a very fine-scale homogeneous assemblage of α-alumina and iron.

Due to welding of the particles during high energy milling, some relatively large agglomerates were formed (≈20 μm diameter). Therefore, the powders were subsequently milled in dry tetrahydrofuran (THF) for 2 h. The resulting slurry was dried with a rotary evaporator. The mean particle size was reduced to 1.7 μm after dispersion in propan-2-ol followed by an ultrasonic treatment. Then the powder was hot-pressed in a graphite die. Heating under vacuum was conducted up to 1700 K. The selected sintering cycle was an initial pressureless heating up to 1000 K (10 K min^{-1}) followed by heating under a constant 30 MPa applied pressure to 1700 K (30 K min^{-1}) with a hold time of 30 min at this temperature. The details of the temperature profiles during the hot-pressing are shown in Fig. 2.

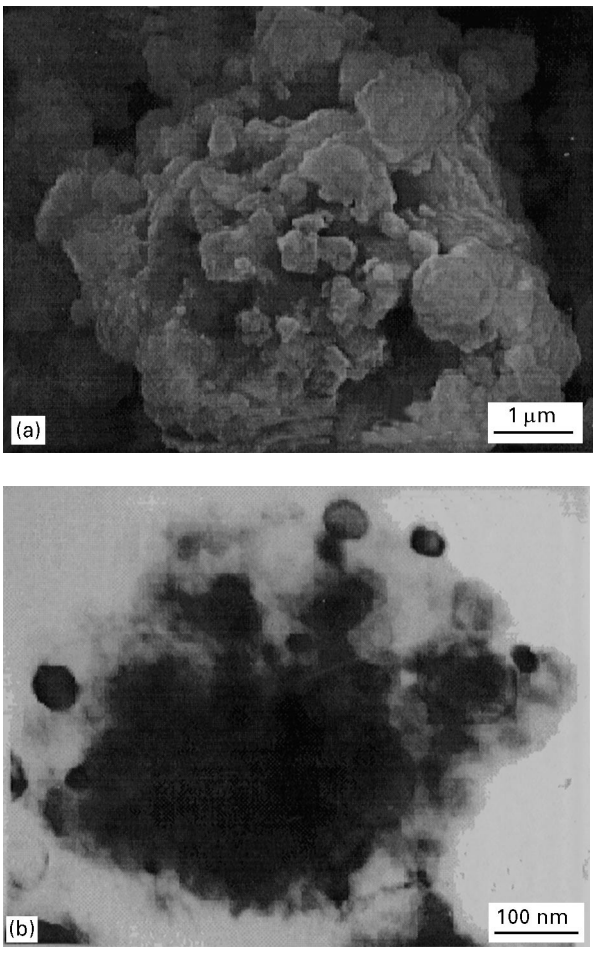

Figure 1 Microstructure of the powder (27 vol% Fe) after an 8 h milling. (a) SEM (b) TEM.

2.2. Sample characterization

Density measurements using the Archimedes' method were made on the as-sintered samples. Microstructural and mechanical characterizations were performed using standard techniques. Dense bars were cut from the as-pressed discs with dimensions of about 3 mm (height), 4 mm (width) and 25 mm (length). The machining damage was mechanically removed by polishing, ultimately with 1 μm diamond paste to produce an optical finish. The edges were chamfered to avoid surface defects located at a specimen edge.

The microstructures were studied by high-magnification optical microscopy (Reichert-Jung), scanning electron microscopy (SEM) (Jeol JSM 6400F) and

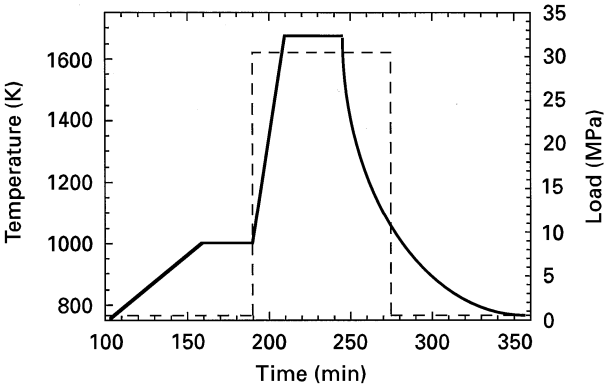

Figure 2 (—) Temperature and (- - -) pressure cycles during hot-pressing.

transmission electron microscopy (TEM) (a Philips CM 120 operated at 120 kV). The surfaces were coated with gold to avoid charging during the SEM observations. No etching was necessary to determine morphological aspects of iron dispersion. The contrast between the two phases was sufficient to obtain good optical micrographs. Composite microstructures were quantitatively analysed (porosity and metallic particle size and morphology) by Visilog image processing (Noesis Vision). For the transmission electron microscopy (TEM) investigations, discs 3 mm in diameter and $\approx 80\,\mu m$ thick were polished, dimpled and ion-beam thinned.

Rupture strength measurements were made with a Zwick machine (model 1446) using the four-point bending method with an inner and outer span of 10 and 20 mm respectively and a displacement rate of $0.1\,mm\,min^{-1}$. The average values were calculated from 3 experiments.

Hardness (HV10) was obtained with a Vickers diamond indenter using a 98 N load and a loading rate of $10\,N\,s^{-1}$. The diagonal of the obtained indentations was much larger ($>100\,\mu m$) than the scale of the microstructure. The accuracy of the measurements was ± 0.5 GPa. Fracture toughness was measured both by the single edge notched beam (SENB) and by the indentation strength techniques [23]. In the latter case the impressions were made on faces parallel to the hot-pressing axis. Beams were then fractured in the four-point bend test with a loading rate of $0.1\,mm\,min^{-1}$. With a high metal content, the materials exhibit lightly plastic fracture behaviours. From the fracture strength, σ_f, and the indent load, P, the fracture toughness is calculated by Equation 2 [23]:

$$K_c = \eta(E/H)^{1/8}(\sigma_f P^{1/3})^{3/4} \quad (2)$$

where E is the Young's modulus, H is the hardness and η is a geometrical constant for which a value of 0.59 was used, as suggested in the literature [23].

The Young's and shear moduli were measured using the ultrasonic transmission method (transductor Panametrics and pulser receiver model 5052 PRX Panametrics).

The room-temperature electrical conductivities of our samples were measured using a four-probe method with separate voltage and current electrodes. Several resistance measurements were performed for each sample by choosing different points on the sample as voltage contacts, and the final resistance of each sample was determined by averaging the measured values. The current–voltage characteristics of all the samples were linear (ohmic) in our measurement conditions.

3. Results and discussion

3.1. Microstructure development

The progress of densification in the various samples during thermal treatment is represented in Fig. 3. Sintering occurs for each composition between 1150–1600 K with comparable kinetics except for the alumina specimen which sinters better and more rapidly. Thus the small amounts of the iron phase interfere with the sintering mechanisms in the matrix, resulting in its partial sintering inhibition. However, raising the sintering temperature up to 1600 K produces dense composites. All the samples achieved a final density higher than 95% of the theoretical value as is reported in Table I.

For all the pellets, a superficial layer with much less metal can be distinguished. The thickness of this layer increases with the metal content up to about 300 μm for the stoichiometric composition. At high temperatures, graphite which came from the die lining, diffuses into the material and combines with iron to form cast iron which has a low melting point temperature (<1550 K). So at higher temperature, under pressure, a fraction of the metallic phase exudes and a layer formed by an alumina skeleton with more porosities appears (Fig. 4a and b). In the following investigations this layer is eliminated by polishing.

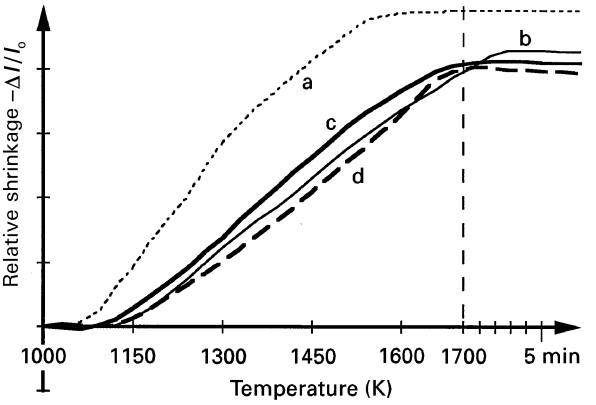

Figure 3 Sintering behaviour of the different compositions during hot-pressing. (a) Pure alumina, (b) 12 vol% Fe, (c) 22 vol% Fe, (d) 36 vol% Fe. Initial dimension of green sample, l_0.

TABLE I Physico-mechanical properties of the composites and also the alumina monolithic reference sample

Composition	Density ($g\,cm^{-3}$)	Relative density (%)	Hardness (GPa)	Young's modulus (GPa)	Shear modulus (GPa)	Fracture strength (MPa)	Inclusion area mean (μm^2)	Fracture toughness ($MPa\,m^{1/2}$)
Al_2O_3 monolith	3.88	97.5	21.2	402	163	350	–	3
+12 vol% Fe	4.25	96.6	16.4	350	141	350	4.5	4.1
+17 vol% Fe	4.50	97.0	14.7	340	136	400	4.6	4.5
+22 vol% Fe	4.78	98.9	11.6	332	132	520	5.4	4.9
+27 vol% Fe	4.85	96.5	9.6	325	129	420	7.1	5.3
+32 vol% Fe	5.00	95.8	8.2	309	122	420	8	5.9
+36 vol% Fe	5.24	97.9	6.4	308	122	430	13	7.8

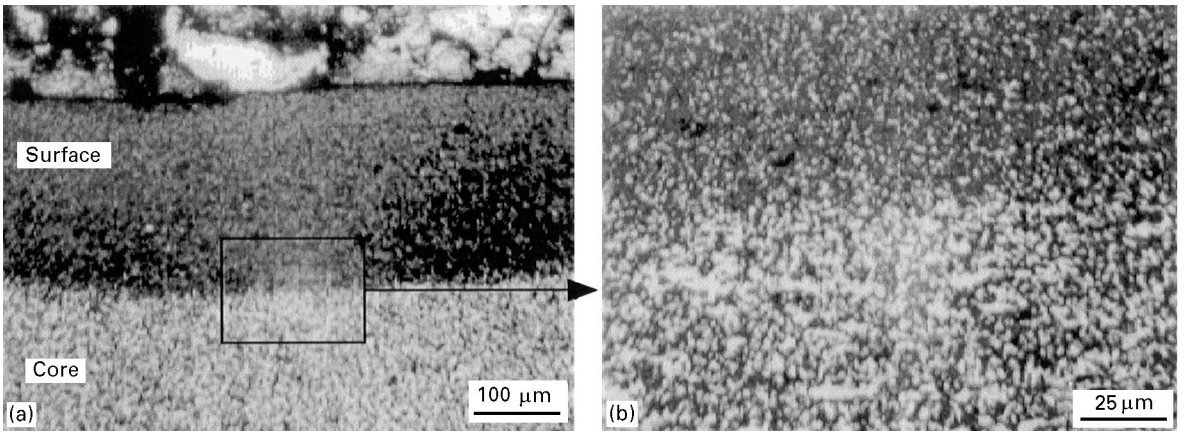

Figure 4 (a) and (b) Optical micrographs of stoichiometric composition.

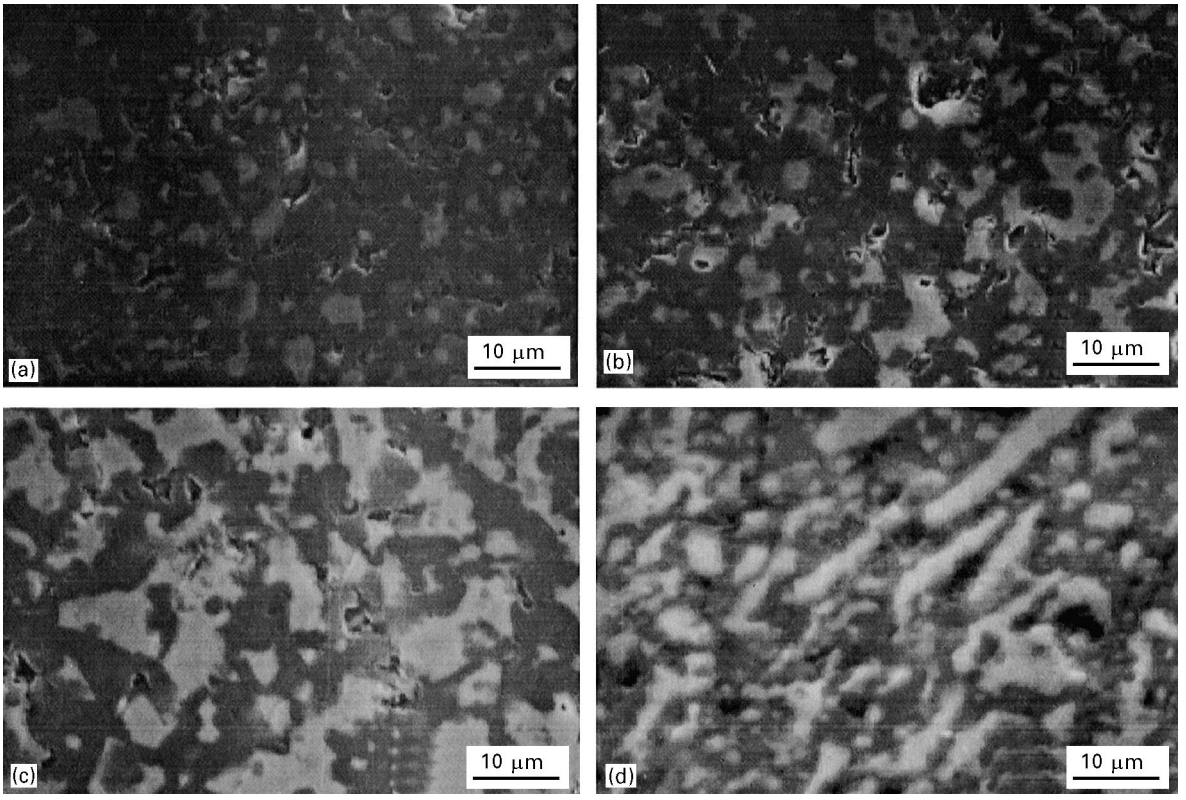

Figure 5 (a–d) SEM microstructures of different sintered specimens. Reactive (a) 17 vol% Fe, (b) 27 vol% Fe, (c) 36 vol% Fe and (d) direct milling 36 vol% Fe.

Typical micrographs of the composite microstructures are shown in Fig. 5(a–d). The Fe areas have bright contrast whilst the alumina grains are grey. To enable comparison of reactive and direct milling, the microstructure of a composite (about 36 vol% Fe) elaborated from milled powder obtained with initially iron and alumina is presented in this figure. The metal inclusions are more elongated and irregular in size and in shape compared to the composites synthesized with reactive milled powders blends. Alumina abrasion makes it difficult to control the final chemical composition. Particles and microporosity appear to be uniformly distributed in the matrix. The materials are homogeneous in that the volume fraction of metal is constant everywhere in the pellets.

Coalescence of the initial iron nano-particles in the mechanosynthesized powder occurs during the thermal consolidation and micrometre sized metal particles with a complex morphology are formed. Nevertheless, a large amount of finer-scale particulates have also been retained and wide inclusion shape and size distributions are observed. For example, in the 22 vol% Fe sample, more than 10% of the metallic iron is distributed over inclusions with an equivalent diameter below 1 μm. Many of the metal inclusions are found as small submicrometre particles especially at low amounts of metal. However at 32–36 vol% Fe the inclusions have a higher size and a more interconnected shape. Whatever the metal amount is, a fine interwoven microstructure between metallic and ceramic phases is always observed. In addition no real differences in the morphology between the different compositions is observed. This is confirmed by study of the metal inclusion geometries. In each studied

composition, the cross-sections of the metal inclusions have a fractal dimension of 1.76 ± 0.02.

These observations may be explained by a similarity in the mechanisms of the metal phase microstructural development. During thermal treatment, the iron nanometre sized particulates which are initially randomly and discretely distributed, on a submicrometre scale, start to coalesce. The larger amount of fine alumina crystallites interfere with this process and partially inhibit metal grain growth and prevent any large sphere-shaped agglomeration. A TEM study (Fig. 6) performed on the stoichiometric composition allows us to estimate the Al_2O_3 mean grain size which is slightly inferior to 1 μm. Very fine submicrometre necks between metal particles are observed (cf. arrows Fig. 7). These results obtained for a high metal-ceramic surface contact, can also be inferred from the fractal dimension.

Figure 6 TEM microstructure of the 36 vol% Fe sample.

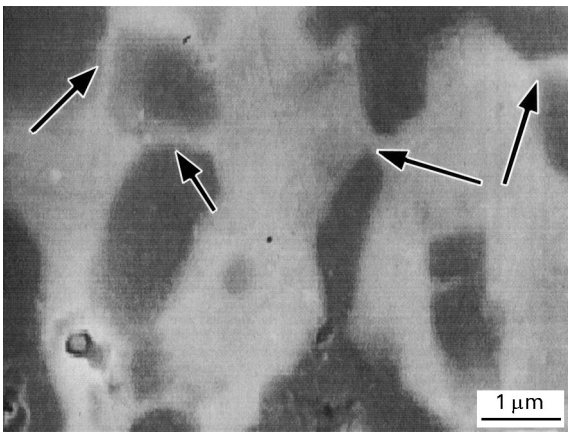

Figure 7 SEM microstructure of the 32 vol% Fe sample.

Iron and alumina display a thermal expansion coefficient mismatch with values of 11 and 6 MK^{-1}, respectively. During cooling a tensile stress is induced which may generate circumferential cracks and interface porosity when the metal particle size exceeds a critical value [14, 15]. Nevertheless, only a small amount of porosity can be observed at the interfaces between metallic particles and the ceramic matrix (even at high metal contents).

In order to obtain more information about the metal distribution, the conductivity of the different composites has been studied. The electrical conductivity changes of the present composites are plotted in Fig. 8a. A sharp transition from insulating to metallic behaviour can be observed at a volume fraction of the metal, near $x_c \approx 0.19$, the so-called percolation concentration.

For ideal metal–insulator composites and above the critical metallic volume fraction x_c, the effective conductivity of the composite σ_{eff} can be expressed in the form:

$$\sigma_{eff} = \sigma_0(x - x_c)^t \quad \text{for } x > x_c \tag{3}$$

where σ_0 is the conductivity of the metallic phase and t the conductivity exponent [24]. Amongst the various parameters that influence the percolation threshold and the conductivity exponent, the most important factors are the metal distribution, the metal shape and the metal-ceramic interactions.

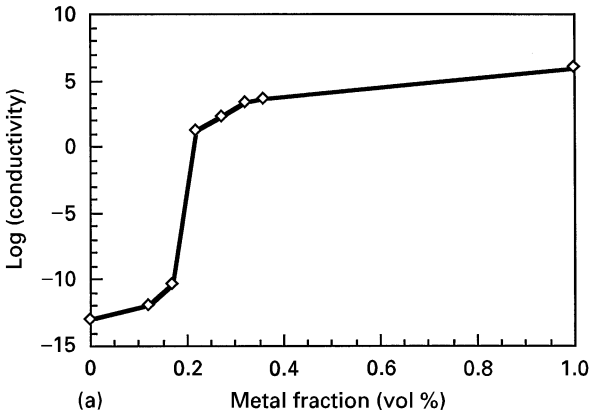

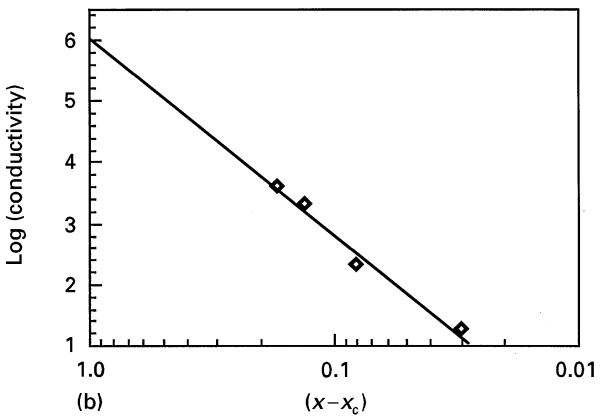

Figure 8 (a) Electrical conductivity as a function of iron content and (b) log–log plot of the conductivity of the composite versus metal fraction.

In order to find the conductivity exponent, we attempted a conventional fit for the series of samples. In fitting our data, shown on the logarithmic plot of Fig. 8b, the critical volume fraction of the metal x_c is 0.19 ± 0.02 and the critical exponent t is 3.2 ± 0.2. The calculated value for σ_0 is $10^6\ \mathrm{S\,cm^{-1}}$, a value which is comparable to the conductivity of pure iron.

Although the percolation concentration is close to the value obtained with statistical percolation models, the large value of the exponent t differs considerably. Such a high value of the critical exponent can be attributed to the complex microstructure of metallic particles and the existence of narrow necks in the conducting paths with multiple contacts between adjacent particles [25]. This is closely related to the microstructure shown in Fig. 7. Lee *et al.* [25] obtained a critical exponent with a value close to 3. Their material consisted of insulating glass spheres that are randomly distributed with a conducting indium phase located in the space between the insulating spheres arrangement. The metal phase was found to form thin necks in such composites, probably in a manner similar to our samples.

3.2. Mechanical behaviour

The main mechanical characteristics of the various Al_2O_3/Fe composites, produced from mechanosynthesized powders are summarized in Table I. The pure alumina specimen has been used as a reference in order to reveal the changes in the mechanical properties due to the metal inclusions. The density of the composite specimens ranged from 96–99% of the theoretical value.

The Young's (E) and shear (G) moduli decrease from $E \approx 400$ GPa and $G \approx 160$ GPa for pure alumina to $E \approx 300 \pm 6$ GPa and $G \approx 120 \pm 3$ GPa at contents of 36 vol% Fe (Fig. 9(a and b)) (for pure iron, $E = 190$ GPa and $G = 70$ GPa). Fig. 9(a and b) show the experimental Young's and shear moduli data. Different laws of mixtures for the composites were used to fit the results as closely as possible, and it is very difficult to characterize the mechanical behaviour by using one single law of mixture. The presence of even small concentrations of porosity can strongly decrease the moduli values as is well known in the case of alumina.

In a recent review paper, Ravichandran [26] propose some theoretical approaches to the prediction of the elastic properties of a two phase material which may be appropriate here. Let us consider a basic unit cell representing the microstructure of the composite. The elastic properties of the unit cell can be derived by using the basic relationships of elastic properties of parallel and series arrangements of two phases respectively loaded in isostrain and isostress configurations.

Considering the microstructures of our metal-ceramic composites, the elastic properties can be approximated by the following relation [26, Equation 9].

$$E_c = \frac{(cE_pE_m + E_m^2)(1+c)^2 - E_m^2 + E_mE_p}{(cE_p + E_m)(1+c)^2} \quad (4)$$

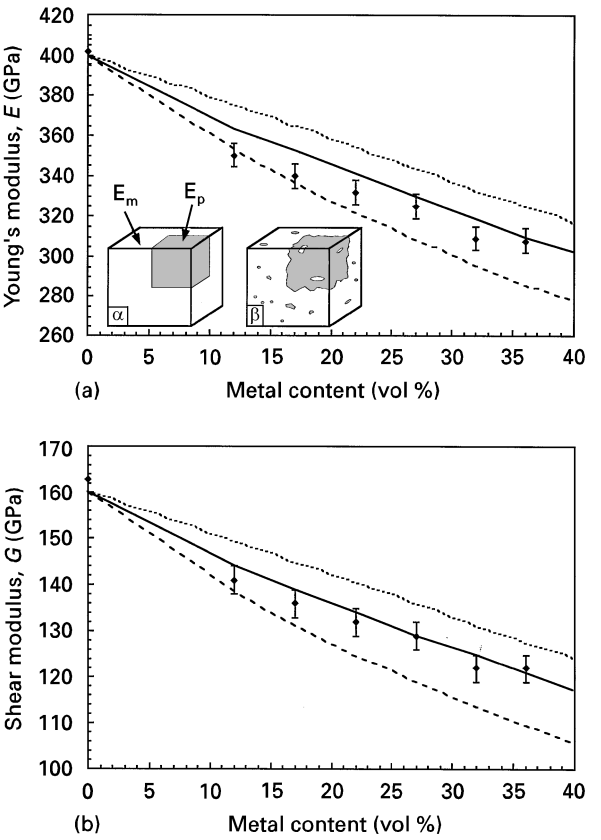

Figure 9 (a) The Young's modulus determined by ultrasonic method, (◆) experimental data and predicted values using: (------) $E_c = V_mE_m + V_pE_p$. (– –) $1/E_c = V_m/E_m + V_p/E_p$ and (—) E_c [26, Equation 9] and (b) the shear modulus determined by ultrasonic method, (◆) experimental data and predicted values using (----) $G_c = V_mG_m + V_pG_p$. (– –) $1/G_c = V_m/G_m + V_p/G_p$ and (—) G_c [26, Equation 9].

with E_p being the Young's modulus of the metal particles, E_m is the matrix Young modulus and c is a parameter which takes into account the particle volume fraction:

$$c = \left(\frac{1}{V_p}\right)^{1/3} - 1 \quad (5)$$

Such a relation was established for the ideal case of the unit cell presented as α on Fig. 9a (the dispersed second phase shown by the grey shaded areas). We assume that it roughly corresponds to our composite microstructures sketched as β on Fig. 9a.

The shear moduli of a two-phase system can be similarly calculated, which result in identical expressions to those for the elastic modulus.

Fig. 9(a and b) show these two theoretical curves. The measured values are slightly lower than the predicted values which can be explained by the presence of residual porosity, imperfect bonding between the phases, and the neglect – as a first approximation – of the influence on E_p and E_m of the submicrometre sized inclusions of the second phase.

The hardness and the fracture toughness of the composites are shown as functions of iron content in Figs 10 and 11, respectively. Due to the softer character of the metal particles, the hardness decreases on increasing the iron content, while the fracture toughness is seen to significantly increase between

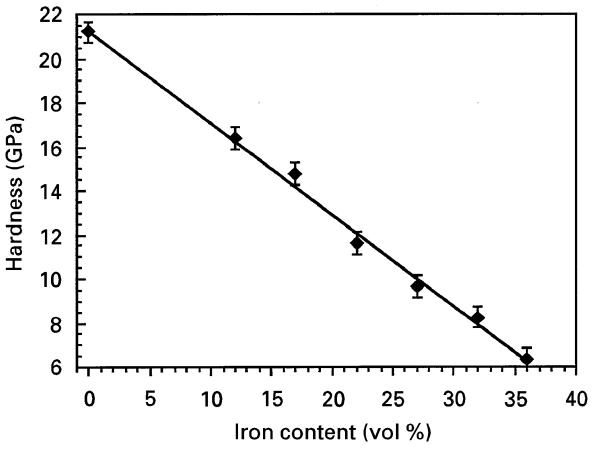

Figure 10 The Vickers hardness of the composites as a function of iron content.

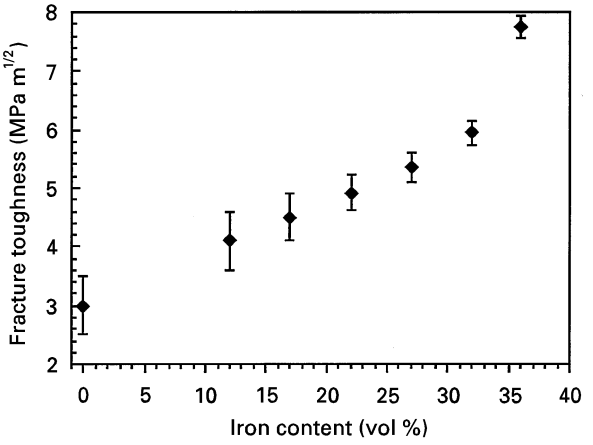

Figure 11 Fracture toughness measured by indentation strength as a function of iron content.

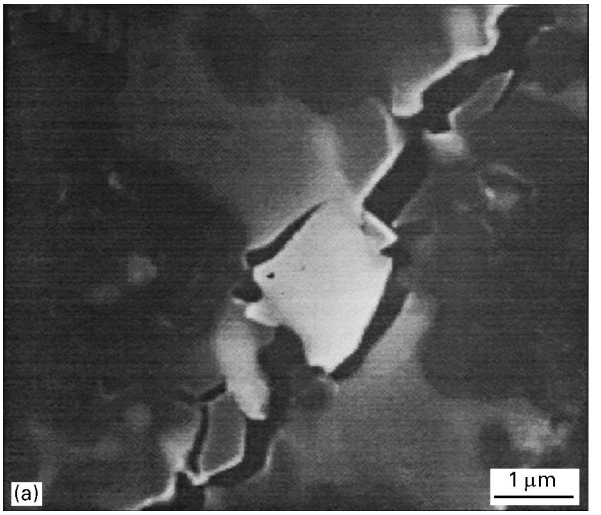

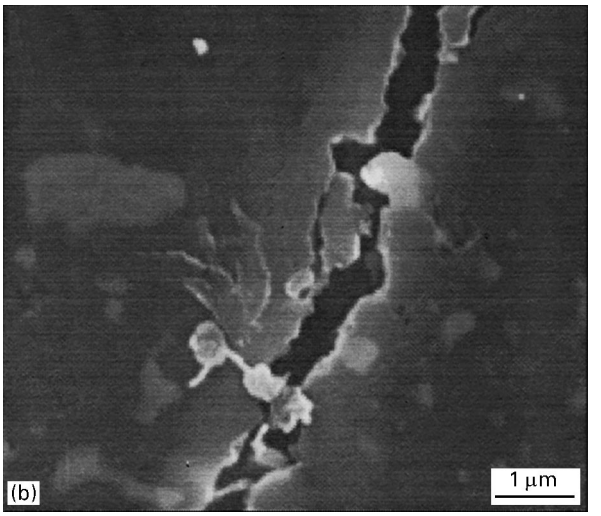

Figure 12 (a) and (b) SEM photographs of indentation cracks propagation in the 27 vol% Fe sample.

3–8 MPa m$^{1/2}$. The fracture strengths of the Al_2O_3/Fe composites exhibit higher values than does the monolithic Al_2O_3 prepared under the same conditions. A maximum value of 520 MPa is observed for the composites containing 22 vol% iron (Table I) which is characterized by the higher relative density.

In general the addition of a second phase dispersion causes an enlargement of the flaw size and a decrease of fracture strength [17], however this type of behaviour has not been observed in these composites. We have calculated the critical flaw size (a_c) from

$$K_{IC} = Y\sigma_R(a_c)^{1/2} \quad (6)$$

where K_{IC} is fracture toughness, σ_R is rupture strength and Y a constant depending on specimen geometry and loading conditions, and found that a_c varies between 25–90 μm. These defects are about 1 order of magnitude larger than the composite microstructure and the mean free paths within either metallic inclusions or ceramic matrix which are only a few micrometres in size. Thus the critical flaws are more likely to result from processing defects rather than being representative of the ultimate performance of such microstructures. Improvements in the quality of processing are expected to yield improvements in the strength.

Stresses induced by thermal expansion mismatch are known to influence the mechanical behaviour of metal/ceramic bonds. Since the linear thermal expansion coefficient of $FeAl_2O_4$ is closer to that of Al_2O_3 (being 7×10^{-6} and 6×10^{-6} K^{-1} respectively), than iron, residual hercynite behaves almost like alumina. The alumina grain size is about 1 μm so we can assume that the influence of the residual stress on toughening the Al_2O_3 phase by microcracking is less important than the contribution from the metallic inclusions [27].

Examples of interactions between a crack and iron inclusions are shown in Fig. 12(a and b). The cracks are either bridged (Fig. 12a), or deflected (Fig. 12b) by the metallic grains. The fracture is mainly intergranular but also runs through some of the metallic grains. It has been observed that the fracture mode and the crack propagation type are locally modified according to the sizes and shapes of the encountered metallic inclusions: i.e., from transgranular with large Fe particles to intergranular with submicrometre Fe inclusions as can be seen on the fracture surfaces (Fig. 13(a and b)). Some entirely decohered grains appear, confirming the deflection of the crack and we can observe stretched metal particles which confirm the plastic

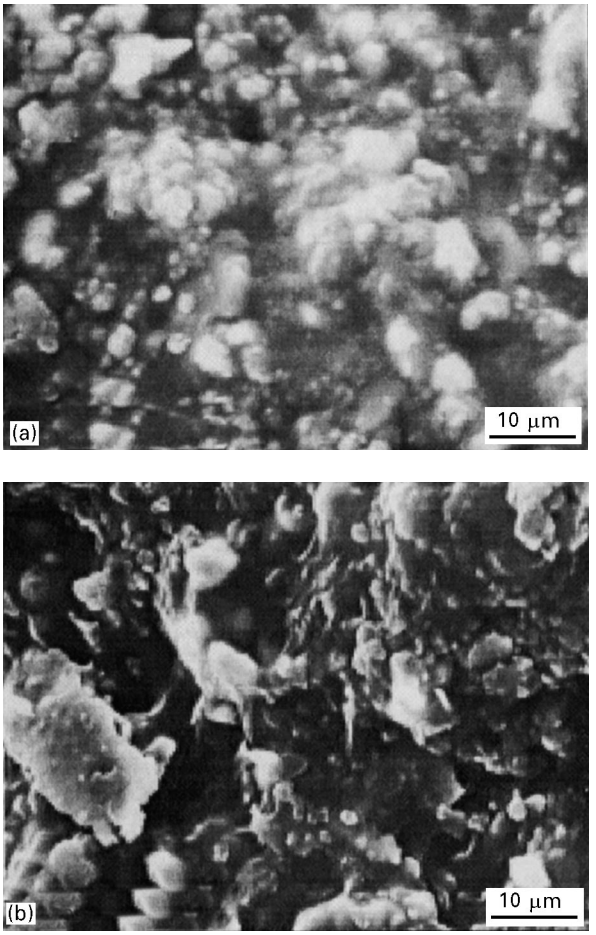

Figure 13 SEM photographs of fractured surfaces (a) 12 vol% Fe and (b) 36 vol% Fe.

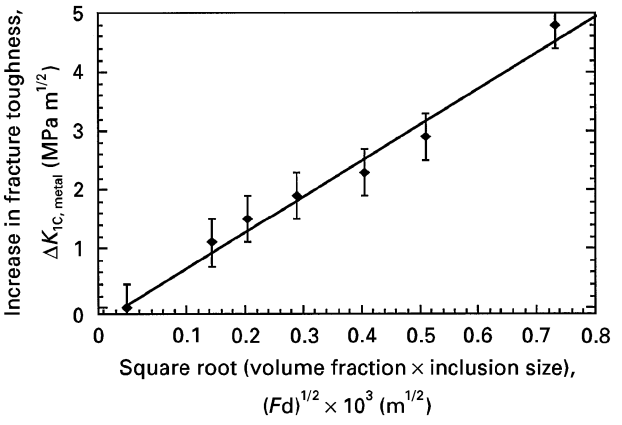

Figure 14 The fracture toughness increase as a function of the square root of the product of volume fraction and inclusion size.

deformation phenomena. The toughness enhancement of the composites is due to a combination of plastic deformation and crack deflection mechanisms.

The deformation behaviour of metallic inclusion in a brittle matrix has been investigated by Ashby *et al.* [11]. They have suggested that the toughness increase, contributed by plastic deformation, ΔK_{IC}, is proportional to the square root of the product of the volume fraction and inclusion size. The experimental results are compiled in Fig. 14 and a linear relationship is found. Such a linear relationship indicates that deflections around metallic inclusions are limited and more significance should be given to the plastic deformation mechanism.

4. Conclusions

Alumina–iron cermets have been fabricated by the hot pressing of nanocomposite mechanosynthesized powders. The materials exhibit a homogeneous dispersion of Fe which is simultaneously achieved at the nanometre and micrometre scales. Interwoven microstructures are observed at large Fe volume fractions. The physical properties of the cermets are directly dependent on the metal content with continuous and fairly linear relationships being obtained between mechanical properties and the iron content up to 36 vol% Fe. Minor differences in the structure and the interfacial characteristics are observed between the specimens containing low or high iron contents. Even at high metal contents, a good contact between the iron particles and the alumina matrix is achieved. Due to such characteristics, significantly improved mechanical properties have been obtained. The presence of the metallic phase induces a toughening by a combination of crack deflection and plastic deformation of the metal particles.

With ranges of fracture toughness between 4–8 MPa m$^{1/2}$, a fracture strength between 350–520 MPa and a hardness between 7–17 GPa, it appears that iron–alumina cermets will be able to compete with other materials for structural applications once their processing conditions have been fully optimized. More generally, it can be concluded that consolidation of mechanosynthesized powders is a simple and efficient method to prepare dense, homogeneous ceramic-metal composites containing high metal contents.

References

1. J. R. TINKLEPAUGH and W. B. CRANDALL, in "Cermets", edited by J. R. Tinklepaugh and W. B. Crandall (Reinhold, New York, 1960).
2. T. S. SHELVIN, *J. Amer. Ceram. Soc.* **37** (1954) 140.
3. M. S. NEWKIRK, A. W. URQUHART and H. R. ZWICKER, *J. Mater. Res.* **1** (1986) 81.
4. D. T. RANKIN, J. J. STIGLICH, D. R. PETRAK and R. RUH, *J. Amer. Ceram. Soc.* **54** (1971) 277.
5. M. NAWA, T. SEKINO and K. NIIHARA, *J. Mater. Sci.* **29** (1994) 3185.
6. P. A. TRUSTY and J. A. YEOMANS, *Ceramic Engng. Sci. Proc.* **14** (1993) 908.
7. W. H. TUAN and R. J. BROOK, *J. Eur. Ceram. Soc.* **6** (1990) 31.
8. E. BREVAL, Z. DENG, S. CHIOU and C. G. PANTANO, *J. Mater. Sci.* **27** (1992) 1464.
9. X. SUN and J. A. YEOMANS, *ibid.* **31** (1996) 875.
10. W. B. CHOU and W. H. TUAN, *J. Eur. Ceram. Soc.* **15** (1995) 291.
11. M. F. ASHBY, F. J. BLUNT and M. BANNISTER, *Acta Metall.* **37** (1989) 1847.
12. L. S. SIGL, P. A. MATAGA, B. J. DALGLEISH, R. M. McMEEKING and A. G. EVANS, *ibid.* **36** (1988) 945.
13. X. ZHANG, G. LU, M. J. HOFFMANN and R. METSELAAR, *J. Eur. Ceram. Soc.* **15** (1995) 225.

14. R. W. DAVIDGE and T. J. GREEN, *J. Mater. Sci.* **3** (1968) 629.
15. R. KOLHE, C. Y. HUI, E. USTUNDAG and S. L. SASS, *Acta Mater.* **44** (1996) 279.
16. M. BANNISTER and M. F. ASHBY, *Acta Metall. Mater.* **39** (1991) 2575.
17. K. NIIHARA, *Seramikkusu Kyokai Gakujutsu Ronbunski* **99** (1991) 974.
18. H. GLEITER, *Prog. Mater. Sci.* **33** (1989) 223.
19. P. MATTEAZZI and G. LE CAER, *J. Amer. Ceram. Soc.* **75** (1992) 2749.
20. D. OSSO, O. TILLEMENT, A. MOCELLIN, G. LE CAER, O. BABUSHKIN and T. LINDBACK, *J. Eur. Ceram. Soc.* **15** (1995) 1207.
21. K. P. THIESSEN, *J. de Chimie Physique* **83** (1986) 717.
22. G. WILLIAMSON and W. H. HALL, *Acta Metall.* **1** (1953) 22.
23. P. CHANTIKUL, G. R. ANSTIS, B. R. LAWN and D. B. MARSHALL, *J. Amer. Ceram. Soc.* **64** (1981) 539.
24. F. LUX, *J. Mater. Sci.* **28** (1993) 285.
25. S.-I. LEE, Y. SONG, T. W. NOH, X.-D. CHEN and J. R. GAINES, *Phys. Rev. B* **34** (1986) 6719.
26. K. S. RAVICHANDRAN, *J. Amer. Ceram. Soc.* **77** (1994) 1178.
27. R. W. RICE and S. W. FREIMAN, *ibid* **64** (1981) 350.

Received 24 October 1996
and accepted 10 February 1997